C60-Adsorbed Single-Walled Carbon Nanotubes as Metal-Free, pH-Universal, and Multifunctional Catalysts for Oxygen Reduction, Oxygen Evolution, and Hydrogen Evolution

Rui Gao,[†,‡,§] Quanbin Dai,[†,§] Feng Du,[†] Dongpeng Yan,[*,‡] and Liming Dai[*,†]

[†]Center of Advanced Science and Engineering for Carbon (Case4Carbon), Department of Macromolecular Sciences and Engineering, Case Western Reserve University, Cleveland, Ohio 44106, United States

[‡]Beijing Key Laboratory of Energy Conversion and Storage Materials, College of Chemistry, Beijing Normal University, Beijing 100875, China

S *Supporting Information*

ABSTRACT: Buckminsterfullerene (C_{60}) was adsorbed onto single-walled carbon nanotubes (SWCNTs) as an electron-acceptor to induce intermolecular charge-transfer with the SWCNTs, leading to a class of new metal-free C_{60}-SWCNT electrocatalysts. For the first time, these newly developed C_{60}-SWCNTs were demonstrated to act as trifunctional metal-free catalysts for oxygen reduction reaction (ORR), oxygen evolution reaction (OER), and hydrogen evolution reaction (HER) over a wide range of pH values, from acid to alkaline, with even higher electrocatalytic activities and better long-term stabilities than those of commercial Pt and RuO_2 counterparts. Thus, the adsorption-induced intermolecular charge-transfer with the C_{60} electron-acceptor can provide a general approach to high-performance, metal-free, pH-universal carbon-based trifunctional metal-free electrocatalysts for water-splitting and beyond.
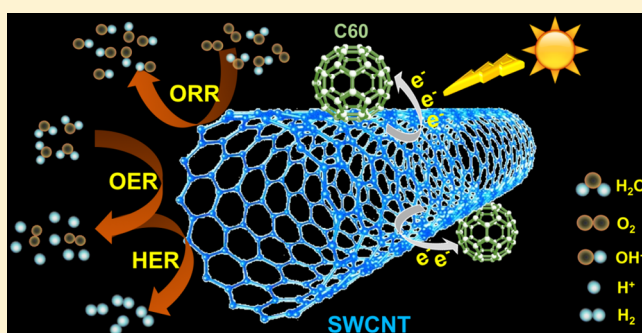
1. INTRODUCTION

Renewable and green energy technologies, such as fuel cells,[1] metal−air batteries,[2] and water-splitting systems,[3] hold great promise toward solving the continuously increasing global energy and environmental challenges. In these energy technologies, three seemingly simple reactions—the hydrogen evolution reaction (HER), oxygen reduction reaction (ORR), and oxygen evolution reaction (OER)—dominate energy conversion and storage processes. However, noble-metal-based catalysts (e.g., Pt, RuO_2, IrO_2) are required to promote the HER to generate hydrogen fuel from photocatalytic/photoelectrochemical water-splitting, the ORR in fuel cells for energy conversion, and the OER in metal−air batteries for energy storage.[2−4] The high cost of precious-metal-based catalysts and their limited reserve have precluded these renewable energy technologies from large-scale commercial applications.[1−5] Therefore, considerable effort has been devoted to the development of non-precious-metal catalysts to completely or partially replace noble-metal catalysts for clean and renewable energy technologies.[6] In this regard, carbon-based metal-free electrocatalysts (C-MFECs) have recently received a great deal of interest due to their multiple advantages of low cost, high efficiency, good long-term stability, and multifunctionality.[2,7]

Since the discovery of the first C-MFEC in 2009,[8] enormous progress has been made and various carbon nanomaterials,

including carbon nanotubes (CNTs), graphene, and carbon quantum dots, doped with heteroatoms (e.g., N, B, S) have been developed for the ORR, OER, and/or HER electrocatalysis.[2,7,9] Besides, various heteroatom-doped carbon composites, such as graphene quantum dots/graphene nanoribbons and graphene/CNT structures, have also been reported for metal-free electrolysis.[10] For ORR, combined experimental and theoretical studies have revealed that the improved catalytic performance of heteroatom-doped carbons could be attributed to the electron-accepting/donating abilities of the heteroatom(s) to create net positive/negative charge(s) on adjacent carbon atoms to change the chemisorption mode of O_2 onto the C-MFECs, which effectively weakens the O−O bonding and facilitates the ORR process.[8,11]

In addition to the intramolecular charge-transfer that imparts ORR electrocatalytic activities to heteroatom-doped carbon nanotubes, graphene, and graphite described above, pure carbon CNTs or graphene, either in an aligned or non-aligned form, adsorbed with certain polyelectrolytes (e.g., PDDA) have also been demonstrated to act as metal-free electrocatalysts for ORR through the *intermolecular* charge-transfer from the all-carbon CNTs or graphene to the adsorbed PDDA[12a,b] or PEDOT.[12c] In particular, we demonstrated that

the PDDA-adsorbed vertically aligned CNT electrode possesses remarkable electrocatalytic properties for ORR,[12b] similar to those of a commercially available Pt/C electrode. These results clearly indicate that the important role of intermolecular charge-transfer to ORR can be applied to carbon nanomaterials in general for the development of various other metal-free efficient ORR catalysts for fuel cell applications, even new catalytic materials for applications beyond fuel cells (e.g., metal−air batteries, electrochemical biosensors). These previous studies prompted us to leverage the strong charge-transfer effects between uncharged C_{60} and CNTs for producing stable and efficient *multifunctional* electrocatalysts largely free from heteroatom-doping and defect, a promising possibility that has not been recognized so far.

Owing to its unique spherical molecular structure, with all sp^2-hybridized carbon atoms, and unparalleled electron affinity, capable of accepting six electrons per C_{60} molecule, buckminsterfullerene (C_{60}) has been widely studied for biomedical and optoelectronic applications.[13] As such, various C_{60}-CNT composites, including C_{60}-encapsulated CNT peapod structures[14] and C_{60}-grafted CNTs,[15] have been developed for electrochemical sensing and many other applications. However, the possible application of C_{60} for electrocatalysis has rarely been discussed in the literature. To our best knowledge, no C_{60}-based multifunctional electro-catalyst has been reported to date.

In this study, we adsorbed C_{60} onto single-walled carbon nanotubes (SWCNTs) to cause intermolecular charge-transfer with SWCNTs, leading to even better electrocatalytic activities than those of commercial Pt and RuO_2 catalysts for ORR, OER, and HER. We further demonstrated that the resultant high-performance C_{60}-SWCNT multifunctional electrocata-lysts are promising for water-splitting[16] and beyond.[17] As schematically shown in Figure 1a, the newly developed C_{60}-SWCNTs can act as both efficient metal-free ORR/OER/HER trifunctional and OER/HER bifunctional catalysts (*vide infra*). Therefore, this work has not only opened up new applications for C_{60} but also provided a facile, but efficient and cost-effective, approach to metal-free, heteroatom-/defect-free multifunctional ORR/OER/HER catalysts simply by adsorbing C_{60} onto SWCNTs.

2. RESULTS AND DISCUSSION

In a typical experiment, the adsorption of C_{60} onto SWCNTs was carried out by simply dispersing SWCNTs in an aqueous solution[18] of C_{60} for different durations (denoted as C_{60}-$SWCNT_n$, n = 5, 10, 15, and 20 min; see Experimental Section). The content of C_{60} in C_{60}-$SWCNT_n$ (n = 5, 10, 15, and 20 min) was monitored by UV−vis absorption measure-ments. As shown in Figure 1b, the intensities of the characteristic absorption bands of the C_{60} solution at 277 and 360 nm,[19] respectively, decreased with increasing n (n = 5, 10, and 15 min), indicating that an increased number of C_{60} molecules were adsorbed onto the SWCNT in C_{60}-$SWCNT_n$ samples with increasing adsorption time (Figure 1c). Over adsorption for 15 min, however, the C_{60} adsorption bands remained unchanged (e.g., C_{60}-$SWCNT_{15}$, C_{60}-$SWCNT_{20}$ in Figure 1b,c), suggesting that the adsorption of C_{60} onto the surface of SWCNTs was saturated after 15 min adsorption in this particular case, and hence the similar amount of adsorbed C_{60} for both the C_{60}-$SWCNT_{15}$ and C_{60}-$SWCNT_{20}$. Figures S1 and S3 show transmission electron microscopy (TEM) images
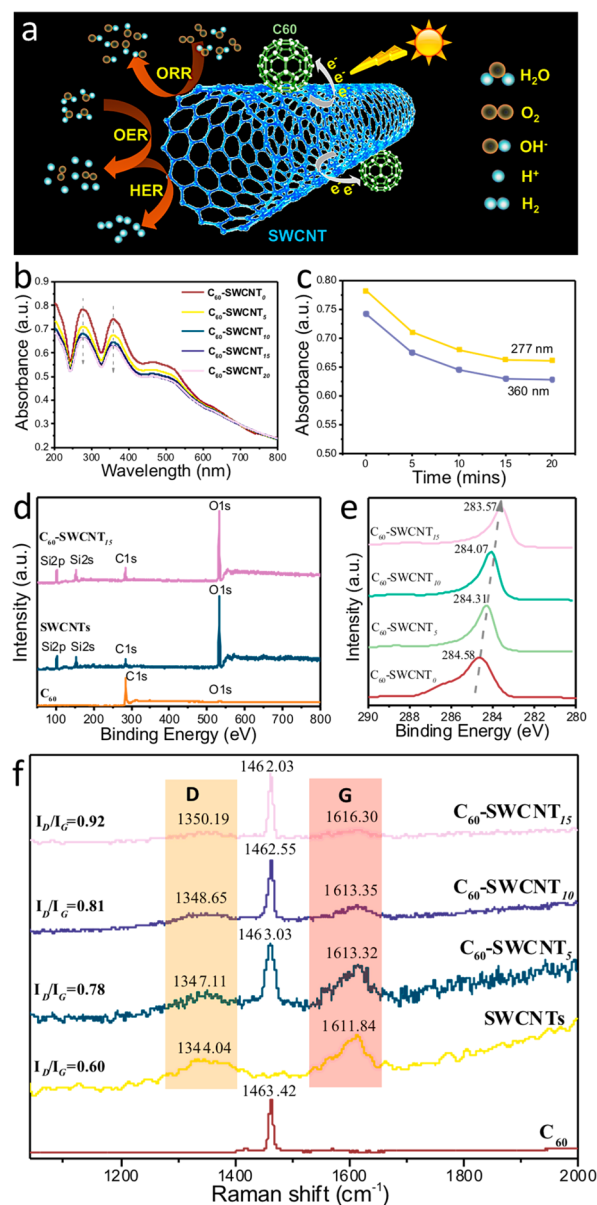

Figure 1. (a) Illustration of charge-transfer process and ORR/OER/HER on C_{60}-SWCNTs. (b) UV−vis absorption spectra of C_{60}-$SWCNT_n$ (n = 0, 5,10,15, and 20 min). (c) Plot of the absorbance intensity as a function of n. (d) XPS survey spectra for SWCNTs before and after the adsorption with C_{60}. Also included is the corresponding spectrum for pure C_{60} as reference. (e) C 1s XPS spectra of C_{60}-$SWCNT_n$ (n = 0, 5, 10, and 15 min). (f) Raman spectra of C_{60} and C_{60}-$SWCNT_n$ (n = 0, 5, 10, and 15 min).

for pure C_{60}, SWCNTs, and the resultant C_{60}-$SWCNT_n$ (n = 5, 10, and 15 min), which revealed a diameter of 1.2 nm for the SWCNT (Figure S1a), as also supported by the radial breathing modes (RBMs) of SWCNTs at 217.3 cm^{-1}, corresponding to a nanotube diameter of 1.14 nm (Figure S2).[20]

Figure S1b reproduces a typical TEM image for pure C_{60} nanoparticles with a diameter of about 1.3 nm, revealing particle features similar to those of the C_{60} nanoparticles in the C_{60}-$SWCNT_n$ (n = 5, 10, 15 min) shown in Figure S3. Other evidence for physical adsorption of C_{60} on SWCNTs comes from FTIR spectra (Figure S4), which show that the FT-IR spectrum of C_{60}-SWCNTs is a simple combination of those for

C_{60} and SWCNTs without any peak position shift, indicating no strong chemical interaction between C_{60} and SWCNTs. The XRD patterns in Figure S5 show that the C_{60}, SWCNTs, and C_{60}-SWCNT$_{15}$ all have a high degree of crystallization, implying a good charge mobility and electrochemical stability for C_{60}-SWCNT$_{15}$ free from heteroatom and defect (Figure 1d−f).[20]

The corresponding X-ray photoelectron spectroscopy (XPS, Figure 1d) clearly verified the absence of any metal elements for SWCNTs produced by the metal-free growth,[9d] but the presence of O and Si apart from C. The O and Si with an atomic ratio of O to Si of 2.11 are from the SiO_2 substrate used for the SWCNTs XPS measurements. XPS and Raman measurements were also performed to confirm the adsorption of C_{60} onto SWCNTs as well as the associated intermolecular charge-transfer. Compared to the C 1s XPS peak for pure C_{60}, the C 1s XPS peak positions for C_{60}-SWCNT$_n$ ($n = 0, 5, 10,$ and 15 min) show a negative shift to lower binding energies with increasing adsorption time n (Figure 1e), indicating the occurrence of charge-transfer from the SWCNTs to C_{60}.[9d] The observed intermolecular charge-transfer was also supported by Raman spectroscopic measurements carried out for the pure SWCNTs before and after adsorption with C_{60}. As expected, the Raman spectrum of SWCNTs displays two prominent peaks at ~1611 and ~1344 cm^{-1} corresponding to the G- and D-bands, respectively, while Raman spectrum of C_{60} shows only one peak at ~1643 cm^{-1}. Raman spectra of C_{60}-SWCNT$_n$ ($n = 5, 10,$ and 15 min) exhibit a slight increase in the intensity ratio of the D-band to the G-band with increasing C_{60} adsorption time (Figure 1f), also accompanied by an upshift of the peak positions. While the upshift in the peak position supports the charge-transfer from SWCNTs to the electron-withdrawing C_{60}, the increase in the peak intensity ratio of the D-band to G-band (I_D/I_G) for C_{60}-SWCNT$_n$ ($n = 5, 10, 15$ min) indicates that the nanotube structure became slightly more disordered via the adsorption-induced charge-transfer to C_{60}.

To investigate electrocatalytic properties, we initially performed the ORR measurements on C_{60}-SWCNT$_n$ ($n = 5, 10,$ and 15 min) in 0.1 M KOH. For comparison, pure C_{60}, pure SWCNTs, and Pt/C (20 wt%, Johnson Matthey) were also measured under the same conditions. Compared with the pure C_{60} (onset potential, $E_{onset} = 0.62$ V, half-wave potential, $E_{1/2} = 0.53$ V, and diffusion-limiting current, $I_{dl} = 0.24$ mA/cm^2) and SWCNTs ($E_{onset} = 0.84$ V, $E_{1/2} = 0.80$ V, and $I_{dl} = 0.32$ mA/cm^2), all the C_{60}-SWCNT$_n$ ($n = 5, 10,$ and 15 min) catalysts showed better ORR performance (Figure S6 and Table S1). These results confirm that charge-transfer between the adsorbed C_{60} and SWCNTs have indeed contributed to the ORR electrocatalytic activity for the C_{60}-SWCNTs. Among all the C_{60}-SWCNT$_n$ ($n = 5, 10,$ and 15 min) samples, the highest ORR activity was observed for C_{60}-SWCNT$_{15}$ in terms of E_{onset} (0.91 V), $E_{1/2}$ (0.84 V), and I_{dl} (1.73 mA/cm^2, Figure S6), presumably due to the lowest charge-transfer resistance (Figure S7) at this mass ratio. Therefore, we focus mainly on the C_{60}-SWCNT$_{15}$ below.

To start with, we carried out cyclic voltammetry (CV) measurements of C_{60}-SWCNT$_{15}$ in a conventional three-electrode electrochemical cell in an O_2- or N_2-saturated 0.1 M aqueous KOH solution. As shown in Figures 2a and S8, a characteristic oxygen reduction peak at 0.86, 0.79, and 0.48 V (versus RHE) was observed for the C_{60}-SWCNT$_{15}$, pure SWCNTs, and C_{60}, respectively, in O_2-saturated 0.1 M
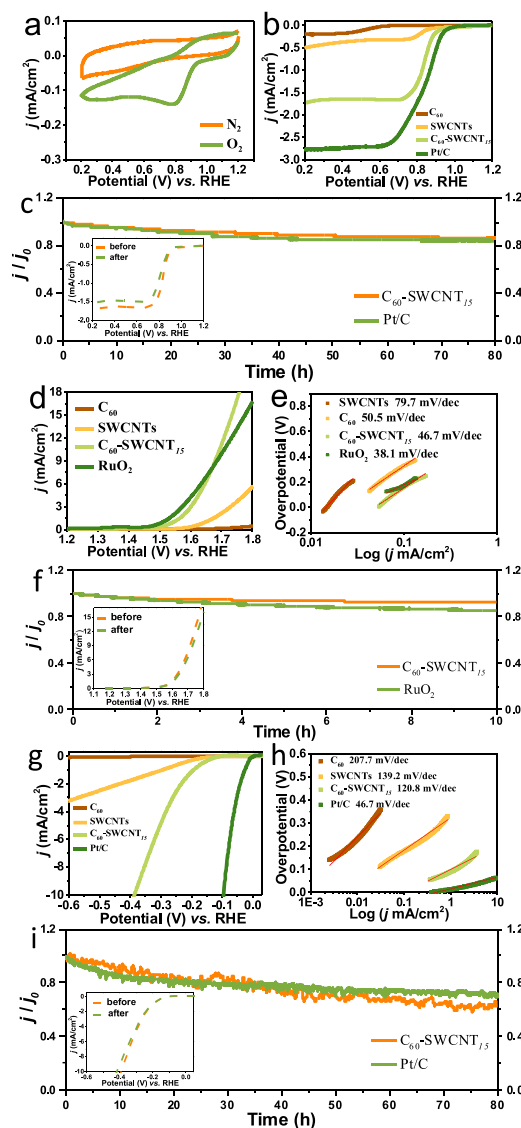
Figure 2. (a) CVs of C_{60}-SWCNT$_{15}$ in an O_2 and N_2-saturated KOH solution (0.1 M). (b) LSVs of ORR for pure C_{60}, SWCNTs, C_{60}-SWCNT$_{15}$, and Pt/C. (c) $I−t$ curve at 0.7 V versus RHE. Inset shows polarization curves before and after 50 h $I−t$ curve. (d) LSVs of OER for pure C_{60}, SWCNTs, C_{60}-SWCNT$_{15}$, and RuO$_2$. (e) The corresponding Tafel plots. (f) $I−t$ curve at 1.7 V versus RHE. Inset shows polarization curves before and after 10 h $I−t$ curve. (g) LSVs of HER for pure C_{60}, SWCNTs, C_{60}-SWCNT$_{15}$, and Pt/C. (h) The corresponding Tafel plots. (i) $I−t$ curve at −0.35 V versus RHE. Inset shows polarization curves before and after 15 h $I−t$ testing. Scan rate: 10 mV s^{-1}.

aqueous KOH, but not in the N_2-saturated electrolyte, indicating a high ORR activity for the C_{60}-SWCNT$_{15}$. Furthermore, the C_{60}-SWCNT$_{15}$ electrode exhibited an excellent stability for the ORR with respect to Pt/C. Figure 2c shows only 7.4% current reduction for the C_{60}-SWCNT$_{15}$ catalyst after a 50 h chronoamperometric test at 0.7 V with O_2 continuously flowing into 0.1 M KOH. However, the Pt/C catalyst lost 9.9% of its initial activity under the same conditions, indicating a higher ORR stability for the C_{60}-SWCNTs than that of the commercial Pt/C (Figure 2c).

To further investigate impacts of the charge-transfer between C_{60} and SWCNTs and to demonstrate the potential

applications of C_{60}-SWCNTs as trifunctional catalysts for ORR, OER, and HER, we also measured the OER performance for C_{60}-SWCNT$_n$ (n = 5, 10, 15 min) samples in a 0.1 M KOH electrolyte. As shown in Figures 2d and S9, C_{60}-SWCNT$_{15}$ exhibited the highest catalytic activity for the OER (Table S2). At 1.69 V potential, the current density of C_{60}-SWCNT$_{15}$ (10 mA cm^{-2}) is 50, 5.3, and 1.2 times higher than those of the pure C_{60}, SWCNTs, and commercial RuO$_2$, respectively (Figure 2d). These observations clearly demonstrated that the charge-transfer from C_{60} to SWCNT has also significantly enhanced the electrocatalytic activity of C_{60}-SWCNTs for OER. Moreover, the C_{60}-SWCNT$_{15}$ electrocatalyst produced a much lower Tafel slope (46.7 mV dec^{-1}) compared with those of the pure C_{60} (50.5 mV dec^{-1}) and SWCNTs electrodes (79.7 mV dec^{-1}), though still slightly higher than that of RuO$_2$ (38.1 mV dec^{-1}), indicating more favorable kinetics toward OER by the C_{60}-SWCNT$_{15}$ electrode (Figure 2e). The steady-state current densities of the C_{60}-SWCNT$_{15}$ show only 7.9% current reduction for 10 h at 1.65 V in 0.1 M KOH electrolyte (Figure 2f), while they remain unchanged at the initial state (inset of Figure 2f). In contrast, 15.1% of the initial activity of RuO$_2$ was lost (Figure 2f) under the same conditions. Remarkably, the C_{60}-SWCNT$_{15}$ exhibited a ΔE of 0.82 V (Figure S10), which is much lower than that of some other carbon-based metal-free materials (e.g., N-graphene/CNT, ΔE = 1.00 V;[21] g-C$_3$N$_4$-carbon-fiber paper, ΔE = 1.06 V[22]).

In addition, HER activities of the C_{60}-SWCNT$_n$ (n = 5, 10, and 15 min) were also investigated in N$_2$-saturated 0.1 M KOH electrolyte using a three-electrode setup. For comparison, we have recorded the linear sweep voltammetry (LSV) curves for the pure C_{60}, SWCNTs, and Pt/C. As shown in Figures 2g and S11, all the C_{60}-SWCNT$_n$ (n = 5, 10, 15 min) catalysts exhibited enhanced catalytic activity compared with the pure C_{60} and SWCNTs. In particular, C_{60}-SWCNT$_{15}$ showed an onset overpotential of ∼114 mV (Table S3). The corresponding Tafel plots (Figure 2h) show a lower Tafel slope (120.8 mV dec^{-1}) for C_{60}-SWCNT$_{15}$ than those of C_{60} (202.7 mV dec^{-1}) and SWCNTs (139.2 mV dec^{-1}), suggesting that the release of molecular hydrogen on the C_{60}-SWCNT$_{15}$ is the rate-limiting step.[17]

The overpotential required to achieve the current density of 10 mA cm^{-2} (Figure 2g) for the C_{60}-SWCNT$_{15}$ and Pt/C are −0.38 and −0.14 V, respectively. Figure 2i displays the polarization curves for the C_{60}-SWCNT$_{15}$ electrode before and after the continuous HER process (15 h), showing only a slight decrease (7.1%) in performance—even more stable than the Pt/C electrode (10.7%). Overall, the C_{60}-SWCNT$_{15}$ catalyst exhibited a low onset potential, high current density, and long-term stability, also promising for HER in the alkaline medium. These results indicate that the C_{60}-SWCNT$_{15}$ is a promising efficient trifunctional catalyst for simultaneous water-splitting and ORR.

As can be seen from the above discussion, the C_{60}-SWCNT catalysts newly developed in this study have been demonstrated to show excellent trifunctional electrocatalytic performance in alkaline media. However, pH values for catalysts to show the best performance for ORR, OER, or HER are usually different.[7e] Unlike most HER electrocatalysts, ORR and OER electrocatalysts often show better performance in an alkaline medium than acidic electrolyte.[7e,10d] This makes it very difficult, if not possible, to develop integrated energy systems for practical applications, for instance, when HER is coupled

with OER in an overall water-splitting process. Therefore, it is important to develop low-cost, pH-universal trifunctional electrocatalysts for effectively catalyzing ORR, OER, and HER simultaneously at any specific pH values.

Compared to alkaline and acidic electrolytes, the benign and harmless pH-neutral medium could simplify the situation for optimization of the ORR, HER, and OER trifunctional electrocatalysts. It is thus highly desirable, though still challenging, to develop efficient trifunctional C-MFECs to achieve high catalytic activities toward OER and HER for overall water-splitting[23] and ORR for microbial fuel cells[24] under neutral conditions. In this regard, we further tested the electrocatalytic performance of C_{60}-SWCNT$_{15}$ for ORR, OER, and HER with a typical three-electrode system in a phosphate buffer solution (pH = 7). As shown in Figures 3a and S12, characteristic oxygen reduction peaks at 0.71, 0.63, and 0.60 V (versus RHE) were observed for the C_{60}-SWCNT$_{15}$, pure SWCNTs, and C_{60}, respectively, in the O$_2$-saturated phosphate buffer solution, but not in the corresponding N$_2$-saturated electrolyte under the same condition. As expected, the C_{60}-SWCNT$_{15}$ exhibited also the highest ORR activity in the neutral phosphate buffer solution. This is also confirmed by the LSV curves shown in Figures 3b and S13, which reveal E_{onset} = 0.81 V, $E_{1/2}$ = 0.77 V, and I_{dl} = 1.31 mA/cm^2 for the C_{60}-SWCNT$_{15}$, outperforming the C_{60}, SWCNTs and other C_{60}-SWCNT$_n$ (n = 5 and 10 min), though still slightly inferior to the Pt/C electrode. Furthermore, Figure 3c shows results from the chronoamperometric test under 0.6 V with continuous O$_2$ flow in the phosphate buffer solution for the C_{60}-SWCNT electrode, revealing only a 6.3% reduction in current from the initial state after a 20 h, which is lower than that of the commercial Pt/C catalyst (a 9.9% loss) under the same condition. As shown in the inset of Figure 3c, the corresponding LSV curves for the C_{60}-SWCNTs remained almost unchanged, indicating that the C_{60}-SWCNTs is also slightly more stable than the commercial Pt/C electrode toward ORR at the neutral pH.

We also tested the OER and HER performance of the C_{60}-SWCNT$_n$ (n = 5, 10, and 15 min) catalysts in the phosphate buffer solution. For comparison, pure C_{60}, pure SWCNTs, Pt/C (20 wt%, Johnson Matthey), and RuO$_2$ were also measured under the same conditions. Figures 3d and S14 show 970, 720, 770, 620, and 480 mV at 10 mA cm^{-2} for the pure C_{60}, pure SWCNTs, C_{60}-SWCNT$_5$, C_{60}-SWCNT$_{10}$, and commercial RuO$_2$, respectively (see also Table S5). In contrast, the C_{60}-SWCNT$_{15}$ electrocatalyst exhibited a relatively low overpotential of 520 mV at 10 mA cm^{-2} with a low onset overpotential of 230 mV (Figure 3d). Notably, the current density of C_{60}-SWCNT$_{15}$ at an overpotential of 600 mV is 20.0 mA cm^{-2}, which is 14.1 and 3.5 times higher than those of the pure C_{60} (1.4 mA cm^{-2}) and SWCNTs (5.8 mA cm^{-2}), respectively, and even superior to the commercial RuO$_2$ (15.5 mA cm^{-2}). The C_{60}-SWCNT$_{15}$ showed a Tafel slope of 129 mV dec^{-1} (Figure 3e), which is comparable to that of the commercial RuO$_2$ (141.1 mV dec^{-1}), but much lower than those of the pure C_{60} (848.2 mV dec^{-1}) and SWCNTs (848.2 and 468.1 mV dec^{-1}). As expected, Figure S15 shows the smallest charge-transfer resistance for C_{60}-SWCNT$_{15}$ among the pure C_{60}, SWCNTs, C_{60}-SWCNT$_5$, and C_{60}-SWCNT$_{10}$. As can be seen in Figure 3f, the catalytic activity of C_{60}-SWCNT$_{15}$, along with the LSV curves (inset of Figure 3f), remained almost unchanged for more than 7.5 h. These results suggest that C_{60}-SWCNT$_{15}$ also exhibited an unprecedentedly
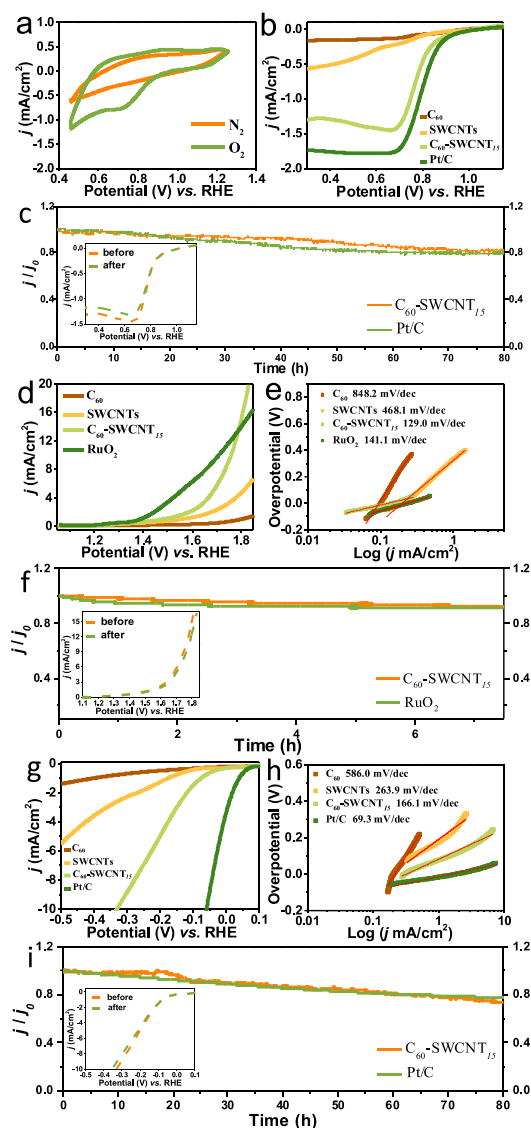
Figure 3. (a) CVs of C_{60}-SWCNT$_{15}$ in an O_2- and N_2-saturated in phosphate buffer solution (pH = 7). (b) LSVs of ORR for pure C_{60}, SWCNTs, C_{60}-SWCNT$_{15}$, and Pt/C. (c) $I-t$ curve at 0.7 V versus RHE. Inset is polarization curves before and after 20 h $I-t$ curve. (d) LSVs of OER for pure C_{60}, SWCNTs, C_{60}-SWCNT$_{15}$, and RuO_2 in phosphate buffer solution. (e) The corresponding Tafel plots. (f) $I-t$ curve at 1.7 V versus RHE. Inset is polarization curves before and after 7.5 h $I-t$ curve. (g) LSVs of HER for pure C_{60}, SWCNTs, C_{60}-SWCNT$_{15}$, and Pt/C in phosphate buffer solution. (h) The corresponding Tafel plots. (i) $I-t$ curve at −0.35 V versus RHE. Inset is polarization curves before and after 15 h $I-t$ testing. Scan rate: 10 mV s^{-1}.

remarkable catalytic activity and stability toward the OER in the neutral medium.

Figures 3g and S16 show the HER LSV curves for all the samples investigated in this study in the neutral phosphate buffer solution. As expected, the pure C_{60} has negligible electrocatalytic activity toward HER, and Pt/C showed the best performance with nearly zero overpotential. C_{60}-SWCNT$_{15}$ exhibited a sharply rising current density with increasing negative potential and a low onset overpotential of 60 mV, suggesting a high HER catalytic activity for the C_{60}-SWCNT$_{15}$. For comparison, the C_{60}-SWCNT$_{15}$ exhibited an

overpotentials of 329 mV at 10 mA cm^{-2}, while the corresponding overpotentials for the pure SWCNTs, C_{60}-SWCNT$_5$, and C_{60}-SWCNT$_{10}$ are 738, 420, and 327 mV, respectively (Table S6). Figure 3h shows the Tafel slopes for the Pt/C electrocatalyst (76.7 mV dec^{-1}), C_{60}-SWCNT$_{15}$ (166.1 mV dec^{-1}), and pure SWCNTs (236.9 mV dec^{-1}) in the neutral medium. The steady-state current density of the C_{60}-SWCNT$_{15}$ shows a small change (8.8%) even after 15 h (Figure 3i), even smaller than the corresponding value of 12% for the Pt/C catalyst, along with the almost unchanged LSV curves for the C_{60}-SWCNT$_{15}$ (inset of Figure 3i). Clearly, therefore, the C_{60}-SWCNT$_{15}$ is also a good metal-free HER catalyst in the neutral medium.

The OER performance of C_{60}-SWCNT$_n$ (n = 5, 10, 15 min) catalysts was also measured in 0.5 M H_2SO_4, for comparison with pure C_{60}, SWCNTs, and commercial RuO_2 catalyst (Table S7). Figures 4a and S17 show an onset potential of ~1.26 V for the C_{60}-SWCNT$_{15}$, which represents an
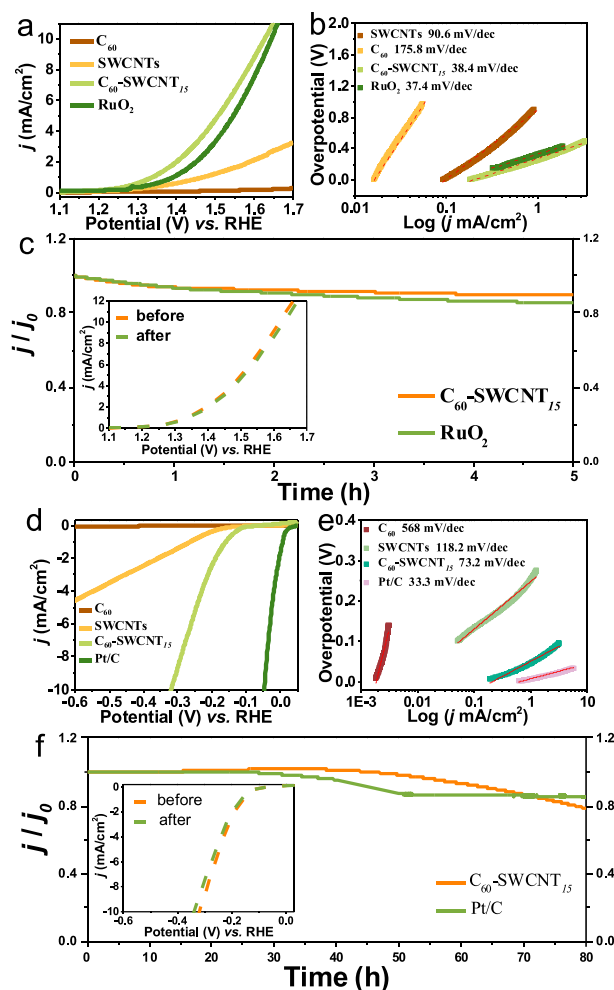

Figure 4. (a) LSVs of OER for pure C_{60}, SWCNTs, C_{60}-SWCNT$_{15}$, and RuO_2 in 0.5 M H_2SO_4 solution. (b) The corresponding Tafel plots. (c) $I-t$ curve at 1.7 V versus RHE. Inset shows polarization curves before and after 1.5 h $I-t$ curve. (d) LSVs of HER for pure C_{60}, SWCNTs, C_{60}-SWCNT$_{15}$, and Pt/C in 0.5 M H_2SO_4 solution. (e) The corresponding Tafel plots. (f) $I-t$ curve at −0.35 V versus RHE. Inset shows polarization curves before and after 20 h $I-t$ testing. Scan rate: 10 mV s^{-1}.

Table 1. ORR, OER, and HER Performance of C_{60}-SWCNT$_{15}$ in Various pH Environments

	E_{onset}(V)	$E_{1/2}$ vs RHE (V)	diffusion-limiting current (mA/cm^2)	Tafel slope (mV/dec)	η at 10 mA cm^{-2} (V)	electrolyte
ORR	0.91	0.84	1.73			0.1 M KOH
OER	0.23			46.7	0.46	0.1 M KOH
HER	0.11			120.8	0.38	0.1 M KOH
ORR	0.81	0.77	1.31			phosphate buffer
OER	0.23			129.0	0.52	phosphate buffer
HER	0.06			166.1	0.33	phosphate buffer
OER	0.03			38.4	0.40	0.5 M H$_2$SO$_4$
HER	0.13			73.2	0.32	0.5 M H$_2$SO$_4$

overpotential of ∼420 mV and is even lower than that of RuO$_2$ catalyst (∼1.28 V, overpotential ∼430 mV). The Tafel slope shown in Figure 4b for the C$_{60}$-SWCNT$_{15}$ is 38.4 mV dec^{-1}, which is similar to that of RuO$_2$ catalyst (37.4 mV dec^{-1}). The steady-state current density of the C$_{60}$-SWCNT$_{15}$ showed a small change (5.0%) even after 1.5 h in 0.5 M H$_2$SO$_4$ (Figure 4c), similar to the corresponding value of 5.4% for the commercial RuO$_2$ catalyst, along with the almost unchanged LSV curves for the C$_{60}$-SWCNT$_{15}$ (inset of Figure 4c). These results indicate a good stability for C$_{60}$-SWCNT$_{15}$ toward OER, even in the acidic medium. The electrocatalytic performance of the C$_{60}$-SWCNT electrode for HER were also measured with a three-electrode configuration in 0.5 M H$_2$SO$_4$. As can be seen in Figures 4d and S18, the pure C$_{60}$ showed almost no catalytic activity, while SWCNT electrode exhibited much better catalytic performance with an onset potential of ∼145 mV and overpotential of 1015 mV at 10 mA cm^{-2} for HER in the acidic medium. Surprisingly, the C$_{60}$-SWCNT$_n$ (n = 0, 5, 10, and 15 min) electrodes showed much improved electrocatalytic performance, in respect to both pure C$_{60}$ and SWCNTs, with a relatively low onset potential of ∼108 and 320 mV overpotential at 10 mA cm^{-2} current (Figure 4d, Table S8). As displayed in Figure 4e, the Tafel slope of C$_{60}$-SWCNT$_{15}$ for HER is 73.2 mV dec^{-1}, which is the smallest among those for the pure C$_{60}$ (568 mV dec^{-1}) and SWCNTs electrocatalysts (118.2 mV dec^{-1}). The observed low Tafel slope indicates a fast HER process for C$_{60}$-SWCNT$_{15}$. The fast OER and HER reaction kinetics of C$_{60}$-SWCNT$_{15}$ is also reflected by the smallest charge-transfer resistance for C$_{60}$-SWCNT$_{15}$ among the pure C$_{60}$, SWCNTs, and C$_{60}$-SWCNT$_n$ (n = 0, 5, 10, and 15 min) (Figure S19). The steady-state current density of the C$_{60}$-SWCNT$_{15}$ showed a small change (2.9%) after 20 h (Figure 4f), even smaller than the corresponding value of 4.4% for the commercial Pt/C catalyst, along with the almost unchanged LSV curves for the C$_{60}$-SWCNT$_{15}$ before and after the chronoamperometric test (inset of Figure 4f). Thus, the C$_{60}$-SWCNT$_{15}$ also showed a superior stability to the Pt/C toward HER in acidic medium. Table 1 summarizes electrocatalytic properties for the C$_{60}$-SWCNT$_{15}$ at various pHs.

To demonstrate potential applications for the C$_{60}$-SWCNT$_{15}$, we investigated a two-electrode electrochemical water-splitting setup, in which the C$_{60}$-SWCNT$_{15}$ was used as both anode and cathode for OER and HER, respectively, in several different electrolyte solutions (e.g., 0.1 M KOH, phosphate buffer solution, and 0.5 M H$_2$SO$_4$). As seen in Figure S21a, the C$_{60}$-SWCNT$_{15}$ HER electrode (with the same C$_{60}$-SWCNT$_{15}$ as the OER counter electrode) showed a small onset potential of −210 mV and a gradually increased current density with increasing potential. In conjunction with the other half of the water-splitting OER reaction (Figure S21b), the

galvanostatic cycling method demonstrated an attractive two electrode water-splitting process for the setup based on the C$_{60}$-SWCNT$_{15}$ bifunctional catalysts, which is comparable to its counterpart based on the Pt/C for ORR and RuO$_2$ for OER. Similar to the control setup, Figure S21c shows a good operation stability for the electrochemical water-splitting setup, in which the C$_{60}$-SWCNT$_{15}$ was used as both the anode and cathode for OER and HER, respectively. H$_2$ bubbles generated from the C$_{60}$-SWCNT$_{15}$ electrode during the water-splitting process could easily leave from the electrode surface (inset Figure S21c) to ensure a long-term stability. C$_{60}$-SWCNT$_{15}$ was also found to show superior water-splitting performance in acidic and neutral media (see Figures S22 and S23).

To gain a better mechanistic understanding of the observed electrocatalytic activities for C$_{60}$-SWCNT$_{15}$ catalysts, we performed energy level diagram analyses (Figure S24). As can be seen in Figure S24, the LUMO level of C$_{60}$ (−4.46 eV) matches well with the energy level for the HER and ORR while the HOMO level of the SWCNTs (−6.38 eV) is favorable for the OER. The bandgaps of the SWCNTs (6.38 to 4.34 eV)[25] and C$_{60}$ (6.30 to 4.46 eV)[26] are in the visible region. Therefore, the formation of the C$_{60}$-SWCNTs junction enabled the observed metal-free electrocatalysis for HER, ORR, and OER as well as the use of visible light to affect the electrocatalytic performance of C$_{60}$-SWCNTs.

To investigate the possible light effects, we used 404.7−579.0 nm visible light (mercury lamp, 1.0 W cm^{-2}) to excite the C$_{60}$-SWCNT$_{15}$. Indeed, it was found that exposure of C$_{60}$-SWCNT$_{15}$ to visible light enhanced electrocatalytic activities for ORR/HER/OER in O$_2$-saturated 0.1 M KOH solution and in phosphate buffer solution (Figures S25 and S26). However, the ORR/HER/OER performance of pure C$_{60}$ and SWCNTs remained unchanged even when they were exposed to the same visible light under the same conditions (Figures S27−S29). Furthermore, the photoinduced current enhancements for the C$_{60}$-SWCNT$_{15}$ were found to be highly reversible and reproducible (Figures S30−S32), showing great potential for practical photoelectrocatalysis. The above observed photo-enhanced electrocatalytic currents are not inconsistent with the photoinduced reduction in the charge-transfer resistance of C$_{60}$-SWCNT$_{15}$, as shown in Figure S33, both of which are, most probably, arising from the light-induced charge-transfer between the intimately contacted C$_{60}$ and SWCNTs (cf. Figure S24).

3. CONCLUSIONS

In summary, we have for the first time demonstrated that the intermolecular charge-transfer between adsorbed C$_{60}$ molecules and SWCNTs largely free from heteroatom and defect can induce high electrocatalytic activities for C$_{60}$-SWCNTs to be used as efficient metal-free trifunctional catalysts for ORR/

OER/HER in alkaline, acid, and neutral electrolytes, though pure C_{60} and SWCNTs do not show any significant catalytic activity. Owing to the photoinduced interfacial charge-transfer in C_{60}-SWCNTs, these newly developed C_{60}-SWCNT metal-free electrocatalysts also show photoresponsive electrocatalytic activities. Furthermore, potential applications of the trifunctional C_{60}-SWCNT metal-free catalysts in overall water-splitting setups of practical significance have been demonstrated. This work has not only opened up new applications for C_{60} but also provided a facile, efficient, and cost-effective way for the development of metal-free, heteroatom-/defect-free, pH-universal multifunctional ORR/OER/HER C_{60}-SWCNT catalysts simply by adsorbing C_{60} onto SWCNTs. It is envisioned that the methodology developed in this work can be applied to the design and development of many other high-performance metal-free catalysts with novel photo-/electro-catalytic properties from physical adsorption between various electron-acceptors and electron-donors.

4. EXPERIMENTAL SECTION

4.1. Catalyst Preparation. A 30-nm-thick SiO_2 film-deposited SiO_2/Si wafer was employed as the substrate. The SiO_2 film deposition was carried out in a reactive dc-magnetron sputtering system using single-crystal SiO_2 as target material (99.99% purity, purchased from Angstrom Sciences, Inc., USA). The plasma treatment was performed using a custom-built reactor, powered by a commercial radio frequency generator. The SiO_2 film-deposited SiO_2/Si wafers were first loaded into the plasma reactor, and water plasma etching was conducted at 250 kHz, 30 W, and 0.62 Torr for 80 min. The plasma-treated wafer was then cleaned by HNO_3 solution (1.0 M), followed by washing with deionized water and acetone under a sonication bath (VWR model 75 D) prior to use.

4.2. Metal-Catalyst-Free Growth of SWCNTs. The synthesis of SWCNTs followed the methods described in our previous work.[9d] The H_2O-plasma-etched SiO_2/Si wafers were first loaded into a small quartz tube (diameter, 10 mm; length, 15 cm). This small tube was then inserted into a reaction quartz tube (diameter, 30 mm; length, 120 cm), which was fixed in a Ceramic Engineering tube furnace (made in Sydney, Australia). Afterward, the substrate was annealed in air at 900 °C for 10 min, and an Ar (1000 sccm) stream was subsequently introduced to exhaust air for 5 min, followed by the introduction of a mixture gas CH_4 (100 sccm)/H_2 (100 sccm) to initiate the growth of SWCNTs. All the gases were controlled by mass flow controllers (MFCs). The growth duration varied from 1 to 20 min. After growth, the furnace was cooled naturally down to room temperature under the protection of Ar/H_2 gas mixture (100/100 sccm).

4.3. Electrode Preparation. C_{60}-SWCNTs were prepared as follows. Briefly, The SiO_2/Si wafers with SWCNTs were initially suspended in 20 mL of de-ionized water by ultrasonication in the presence of C_{60} with the concentration of 1.96 mol/L for 5, 10, 15, and 20 min.

4.4. Characterization. Electrochemical measurements were performed using a computer-controlled potentiostat (CHI 760C, CH Instrument, USA) with a typical three-electrode cell. A platinum wire was used as counter electrode and saturated calomel electrode (SCE) as reference electrode. All the experiments were conducted at room temperature (25 ± 1 °C). X-ray photoelectron spectroscopy (XPS) measurements were performed on a VG Microtech ESCA 2000 using a monochromic Al X-ray source (97.9 W, 93.9 eV). The Raman spectra were collected by Raman spectroscopy (Renishaw), using a 514 nm laser. TEM images were recorded with Philips Tecnai 20 and JEOL JEM-2010 high-resolution transmission electron microscopes. The accelerating voltage was 200 kV in each case.

ORR, HER, and OER were tested in a three-electrode cell, and overall water-splitting was performed on a CHI760C electrochemical workstation in a two-electrode setup. A Pt wire was used as the counter electrode. Saturated calomel electrode was selected as the reference electrode. For the benchmark control, Pt/C was used as the negative electrode and RuO_2 as the positive electrode. All of the electrochemical tests were performed at room temperature of ca. 25 °C. All of the potentials and voltages are iR-corrected, calibrated, and converted to reversible hydrogen electrode. The glassy carbon disk was rinsed with double-distilled water and dried at room temperature before the catalyst was loaded to the disk.

The electrochemical experiments were carried out in O_2-/N_2-saturated electrolyte for ORR/OER/HER. Cyclic voltammetry (CV) curves for the ORR evaluation were recorded by applying a linear potential scan at a sweep rate of 10 mV s^{-1} after purging O_2 or N_2 gas for 30 min. The cycling was repeated until the reproducible CV curves were obtained before the measurements. All electrochemical experiments were performed at 25 ± 1 °C.

■ ASSOCIATED CONTENT

Ⓢ Supporting Information

The Supporting Information is available free of charge on the ACS Publications website at DOI: 10.1021/jacs.9b05006.

Experimental details, Raman, TEM, and XPS characterization, and electrochemical test results, including Figures S1−S35 and Tables S1−S (PDF)

■ AUTHOR INFORMATION

Corresponding Authors
*yandp@bnu.edu.cn
*liming.dai@case.edu

ORCID Ⓘ
Liming Dai: 0000-0001-7536-160X

Author Contributions
§R.G. and Q.D. contributed equally.

Notes
The authors declare no competing financial interest.

■ ACKNOWLEDGMENTS

■ REFERENCES

(1) (a) Yu, W.; Porosoff, M. D.; Chen, J. G. Review of Pt-Based Bimetallic Catalysis: From Model Surfaces to Supported Catalysts. *Chem. Rev.* **2012**, *112*, 5780−5817. (b) Suntivich, J.; May, K. J.; Gasteiger, H. A.; Goodenough, J. B.; Shao-Horn, Y. A Perovskite Oxide Optimized for Oxygen Evolution Catalysis from Molecular Orbital Principles. *Science* **2011**, *334*, 1383−1385. (c) Hu, C. G.; Cheng, H. H.; Zhao, Y.; Hu, Y.; Liu, Y.; Dai, L. M.; Qu, L. T. Newly-Designed Complex Ternary Pt/PdCuNanoboxes Anchored on Three-Dimensional Graphene Framework for Highly Efficient Ethanol Oxidation. *Adv. Mater.* **2012**, *24*, 5493−5498. (d) Steele, B. C. H.; Heinzel, A. Materials for fuel-cell technologies. *Nature* **2001**, *414*, 345−352.

(2) (a) Zhang, J. T.; Xia, Z. H.; Dai, L. M. Carbon-based electrocatalysts for advanced energy conversion systems. *Sci. Adv.* **2015**, *1*, No. e1500564. (b) Li, Q.; Cao, R. G.; Cho, J.; Wu, G. Nanocarbon Electrocatalysts for Oxygen Reduction in Alkaline Media for Advanced Energy Conversion and Storage. *Adv. Energy Mater.* **2014**, *4*, 1301415. (c) Wang, X.; Vasileff, A.; Jiao, Y.; Zheng, Y.; Qiao, S. Z. Electronic and structural engineering of carbon-based metal-free electrocatalysts for water splitting. *Adv. Mater.* **2019**, *31*, 1803625.

(3) (a) Wang, H. T.; Lee, H.-W.; Deng, Y.; Lu, Z. Y.; Hsu, P.-C.; Liu, Y. Y.; Lin, D. C.; Cui, Y. Bifunctional non-noble metal oxide nanoparticle electrocatalysts through lithium-induced conversion for overall water splitting. *Nat. Commun.* **2015**, *6*, 7261. (b) Wang, J. H.; Cui, W.; Liu, Q.; Xing, Z. C.; Asiri, A. M.; Sun, X. P. Recent Progress in Cobalt-Based Heterogeneous Catalysts for Electrochemical Water Splitting. *Adv. Mater.* **2016**, *28*, 215−230. (c) Zheng, Y.; Jiao, Y.; Vasileff, A.; Qiao, S. Z. The hydrogen evolution reaction in alkaline solution: from theory, single crystal models, to practical electrocatalysts. *Angew. Chem., Int. Ed.* **2018**, *57*, 7568−7579. (d) Vasileff, A.; Zheng, Y.; Qiao, S. Z. Carbon solving carbon's problems: recent progress of nanostructured carbon-based catalysts for the electrochemical reduction of CO_2. *Adv. Energy Mater.* **2017**, *7*, 1700759.

(4) (a) Li, J.; Xi, Z.; Pan, Y. T.; Spendelow, J. S.; Duchesne, P. N.; Su, D.; Li, Q.; Yu, C.; Yin, Z.; Shen, B.; Kim, Y. S.; Zhang, P.; Sun, S. Fe Stabilization by Intermetallic $L1_0$-FePt and Pt Catalysis Enhancement in $L1_0$-FePt/Pt Nanoparticles for Efficient Oxygen Reduction Reaction in Fuel Cells. *J. Am. Chem. Soc.* **2018**, *140*, 2926−2932. (b) Petrykin, V.; Macounova, K.; Shlyakhtin, O.; Krtil, P. Tailoring the Selectivity for Electrocatalytic Oxygen Evolution on Ruthenium Oxides by Zinc Substitution. *Angew. Chem., Int. Ed.* **2010**, *49*, 4813−4815. (c) Zheng, Y.; Jiao, Y.; Zhu, Y.; Li, L. H.; Han, Y.; Chen, Y.; Jaroniec, M.; Qiao, S. Z. High Electrocatalytic Hydrogen Evolution Activity of an Anomalous Ruthenium Catalyst. *J. Am. Chem. Soc.* **2016**, *138*, 16174−16181.

(5) (a) Cabán-Acevedo, M.; Stone, M. L.; Schmidt, J. R.; Thomas, J. G.; Ding, Q.; Chang, H. C.; Tsai, M. L.; He, J. H.; Jin, S. Efficient hydrogen evolution catalysis using ternary pyrite-type cobalt phosphosulphide. *Nat. Mater.* **2015**, *14*, 1245−1251. (b) Tian, J. Q.; Liu, Q.; Cheng, N. Y.; Asiri, A. M.; Sun, X. Self-Supported Cu_3P Nanowire Arrays as an Integrated High-Performance Three-Dimensional Cathode for Generating Hydrogen from Water. *Angew. Chem., Int. Ed.* **2014**, *53*, 9577−9581.

(6) (a) Gorlin, M.; Ferreira de Araujo, J.; Schmies, H.; Bernsmeier, D.; Dresp, S.; Gliech, M.; Jusys, Z.; Chernev, P.; Kraehnert, R.; Dau, H.; Strasser, P. Tracking Catalyst Redox States and Reaction Dynamics in Ni−Fe Oxyhydroxide Oxygen Evolution Reaction Electrocatalysts: The Role of Catalyst Support and Electrolyte pH. *J. Am. Chem. Soc.* **2017**, *139*, 2070−2082. (b) Yang, Z.; Zhang, J.; Kintner-Meyer, M. C. W.; Lu, X.; Choi, D.; Lemmon, J. P.; Liu, J. Electrochemical Energy Storage for Green Grid. *Chem. Rev.* **2011**, *111*, 3577−3613. (c) Montoya, J. H.; Seitz, L. C.; Chakthranont, P.; Vojvodic, A.; Jaramillo, T. F.; Nørskov, J. K. Materials for solar fuels and chemicals. *Nat. Mater.* **2017**, *16*, 70−81. (d) Chu, S.; Cui, Y.; Liu, N. The path towards sustainable energy. *Nat. Mater.* **2017**, *16*, 16−22.

(7) (a) Hu, C.; Dai, L. Multifunctional Carbon-Based Metal-Free Electrocatalysts for Simultaneous Oxygen Reduction, Oxygen Evolution, and Hydrogen Evolution. *Adv. Mater.* **2017**, *29*, 1604942−1604950. (b) Qu, L.; Liu, Y.; Baek, J.-B.; Dai, L. Nitrogen-Doped Graphene as Efficient Metal-Free Electrocatalyst for Oxygen Reduction in Fuel Cells. *ACS Nano* **2010**, *4*, 1321−1326. (c) Shui, J.; Du, F.; Xue, C.; Li, Q.; Dai, L. Vertically Aligned N-Doped Coral-like Carbon Fiber Arrays as Efficient Air Electrodes for High-Performance Nonaqueous Li−O_2 Batteries. *ACS Nano* **2014**, *8*, 3015−3022. (d) Zhang, J.; Dai, L. Heteroatom-Doped Graphitic Carbon Catalysts for Efficient Electrocatalysis of Oxygen Reduction Reaction. *ACS Catal.* **2015**, *5* (12), 7244−7253. (e) Dai, L.; Xue, Y. H.; Qu, L.; Choi, H.-J.; Baek, J.-B. Metal-Free Catalysts for Oxygen Reduction Reaction. *Chem. Rev.* **2015**, *115* (11), 4823−4892.

(8) Gong, K.; Du, F.; Xia, Z.; Durstock, M.; Dai, L. Nitrogen-Doped Carbon Nanotube Arrays with High Electrocatalytic Activity for Oxygen Reduction. *Science* **2009**, *323*, 760−764.

(9) (a) Zhang, J.; Dai, L. Nitrogen, Phosphorus, and Fluorine Tri-doped Graphene as a Multifunctional Catalyst for Self-Powered Electrochemical Water Splitting. *Angew. Chem., Int. Ed.* **2016**, *55*, 13296−13300. (b) Li, Q.; Zhang, S.; Dai, L.; Li, L.-S. Nitrogen-Doped Colloidal Graphene Quantum Dots and Their Size-Dependent Electrocatalytic Activity for the Oxygen Reduction Reaction. *J. Am. Chem. Soc.* **2012**, *134* (46), 18932−18935. (c) Yu, D.; Zhang, Q.; Dai,

L. Highly Efficient Metal-Free Growth of Nitrogen-Doped Single-Walled Carbon Nanotubes on Plasma-Etched Substrates for Oxygen Reduction. *J. Am. Chem. Soc.* **2010**, *132* (43), 15127−15129. (d) Xiong, W.; Du, F.; Liu, Y.; Perez, A.; Supp, M.; Ramakrishnan, T. S.; Dai, L.; Jiang, L. 3-D Carbon Nanotube Structures Used as High Performance Catalyst for Oxygen Reduction Reaction. *J. Am. Chem. Soc.* **2010**, *132* (45), 15839−15841. (e) Hu, C.; Dai, L. Doping of Carbon Materials for Metal-Free Electrocatalysis. *Adv. Mater.* **2019**, *31*, 1804672.

(10) (a) Zhang, J.; Zhao, Z.; Xia, Z.; Dai, L. A metal-free bifunctional electrocatalyst for oxygen reduction and oxygen evolution reactions. *Nat. Nanotechnol.* **2015**, *10*, 444−452. (b) Hu, C.; Dai, L. Carbon-Based Metal-Free Catalysts for Electrocatalysis beyond the ORR. *Angew. Chem., Int. Ed.* **2016**, *55*, 11736−11758. (c) Dai, L. Carbon-based catalysts for metal-free electrocatalysis. *Curr. Opin. Electrochem.* **2017**, *4*, 18−25. (d) Liu, X.; Dai, L. Carbon-based metal-free catalysts. *Nat. Rev. Mater.* **2016**, *1*, 16064. (e) Liu, L.; Zeng, G.; Chen, J.; Bi, L.; Dai, L.; Wen, Z. N-doped porous carbon nanosheets as pH-universal ORR electrocatalyst in various fuel cell devices. *Nano Energy* **2018**, *49*, 393−402. (f) Ren, G.; Gao, L.; Teng, C.; Li, Y.; Yang, H.; Shui, J.; Lu, X.; Zhu, Y.; Dai, L. Ancient Chemistry "Pharaoh's Snakes" for Efficient Fe-/N-Doped Carbon Electrocatalysts. *ACS Appl. Mater. Interfaces* **2018**, *10*, 10778−10785.

(11) (a) Zheng, Y.; Jiao, Y.; Li, L. H.; Xing, T.; Chen, Y.; Jaroniec, M.; Qiao, S. Z. Toward Design of Synergistically Active Carbon-Based Catalysts for Electrocatalytic Hydrogen Evolution. *ACS Nano* **2014**, *8*, 5290−5296. (b) Jiang, H.; Zhu, Y.; Su, Y.; Yao, Y.; Liu, Y.; Yang, X.; Li, C. Highly dual-doped multilayer nanoporous graphene: efficient metal-free electrocatalysts for the hydrogen evolution reaction. *J. Mater. Chem. A* **2015**, *3*, 12642−12645. (c) Gong, X.; Liu, S.; Ouyang, C.; Strasser, P.; Yang, R. Nitrogen- and Phosphorus-Doped Biocarbon with Enhanced Electrocatalytic Activity for Oxygen Reduction. *ACS Catal.* **2015**, *5* (2), 920−927. (d) Wei, L.; Karahan, H. E.; Goh, K.; Jiang, W.; Yu, D.; Birer, OÖ.; Jiang, R.; Chen, Y. A high-performance metal-free hydrogen-evolution reaction electrocatalyst from bacterium derived carbon. *J. Mater. Chem. A* **2015**, *3*, 7210−7214.

(12) (a) Wang, S.; Yu, D.; Dai, L.; Chang, D. W.; Baek, J.-B. Polyelectrolyte-Functionalized Graphene as Metal-Free Electrocatalysts for Oxygen Reduction. *ACS Nano* **2011**, *5* (8), 6202−6209. (b) Wang, S.; Yu, D.; Dai, L. Polyelectrolyte Functionalized Carbon Nanotubes as Efficient Metal-free Electrocatalysts for Oxygen Reduction. *J. Am. Chem. Soc.* **2011**, *133*, 5182−5185. (c) Hajova, H.; Kominkova, Z.; Santidrian, A.; Frank, O.; Kubac, L.; Josefik, F.; Kalbac, M. Preparation and Charge-Transfer Study in a Single-Walled Carbon Nanotube Functionalized with Poly(3,4-ethylenedioxythiophene). *J. Phys. Chem. C* **2015**, *119* (37), 21538−21546.

(13) (a) McCreery, R. L. Carbon Electrodes: Structural Effects on Electron-Transfer Kinetics. In *Electroanalytical Chemistry: A Series of Advances*; Bard, A. J., Ed.; Marcel Dekker: New York, 1991; Vol. 17, p 230. (b) Fukuzumi, S.; Guldi, D. M. Electron-Transfer Chemistry of Fullerenes. In *Electron Transfer in Chemistry*; Balzani, V., Ed.; Wiley-VCH:Weinheim, 2001; Vol. 2, p 270. (c) Echegoyen, L.; Echegoyen, L. E. The Electrochemistry of C_{60} and Related Compounds. In *Organic Electrochemistry*; Lund, H.; Hammerich, O., Eds.; Marcel Dekker: New York, 2001; p 323. (d) Liu, Q.; Cui, Q.; Li, X. J.; Jin, L. The applications of buckminsterfullerene C_{60} and derivatives in orthopaedic research. *Connect. Tissue Res.* **2014**, *55*, 71−79. (e) Prato, M.; Maggini, M. Fulleropyrrolidines: A Family of Full-Fledged Fullerene Derivatives. *Acc. Chem. Res.* **1998**, *31* (9), 519−526. (f) Sariciftci, N. S.; Smilowitz, L.; Heeger, A. J.; Wudl, F. Photoinduced Electron Transfer from a Conducting Polymer to Buckminsterfullerene. *Science* **1992**, *258*, 1474−1476. (g) Liu, Z.-B.; Xu, Y.-F.; Zhang, X.-Y.; Zhang, X.-L.; Chen, Y.-S.; Tian, J.-G. Porphyrin and Fullerene Covalently Functionalized Graphene Hybrid Materials with Large Nonlinear Optical Properties. *J. Phys. Chem. B* **2009**, *113* (29), 9681−9686.

(14) Barzegar, H. R.; Gracia-Espino, E.; Yan, A.; Ojeda-Aristizabal, C.; Dunn, G.; Wagberg, T.; Zettl, A. C_{60}/Collapsed Carbon Nanotube Hybrids: A Variant of Peapods. *Nano Lett.* **2015**, *15* (2), 829−834.

(15) (a) Mazloum-Ardakani, M.; Khoshroo, A. High performance electrochemical sensor based on fullerene-functionalized carbon nanotubes/ionic liquid: Determination of some catecholamines. *Electrochem. Commun.* **2014**, *42*, 9−12. (b) Thirumalraj, B.; Palanisamy, S.; Chen, S.-M.; Lou, B.-S. Preparation of highly stable fullerene C60 decorated graphene oxide nanocomposite and its sensitive electrochemical detection of dopamine in rat brain and pharmaceutical samples. *J. Colloid Interface Sci.* **2016**, *462*, 375−381.

(16) Zhang, J.; Dai, L. Nitrogen, Phosphorus, and Fluorine Tri-doped Graphene as a Multifunctional Catalyst for Self-Powered Electrochemical Water Splitting. *Angew. Chem., Int. Ed.* **2016**, *55*, 13296−13300.

(17) Paul, R.; Zhu, L.; Chen, H.; Qu, J.; Dai, L. Recent Advances in Carbon-Based Metal-Free Electrocatalysts. *Adv. Mater.* **2019**, *31*, 1806403.

(18) (a) Priyadarsini, K. I.; Mohan, H.; Mittal, J. P.; Guldi, D. M.; Asmus, K. D. Pulse radiolysis studies on the redox reactions of aqueous solutions of γ-cyclodextrine/C_{60} complexes. *J. Phys. Chem.* **1994**, *98*, 9565−9569. (b) Prylutskyy, Y. I.; Petrenko, V. I.; Ivankov, O. I.; Kyzyma, O. A.; Bulavin, L. A.; Litsis, O. O.; Evstigneev, M. P.; Cherepanov, V. V.; Naumovets, A. G.; Ritter, U. On the Origin of C_{60} Fullerene Solubility in Aqueous Solution. *Langmuir* **2014**, *30*, 3967−3970.

(19) Kato, H.; Nakamura, A.; Takahashi, K.; Kinugasa, S. Size effect on UV-Vis absorption properties of colloidal C_{60} particles in water. *Phys. Chem. Chem. Phys.* **2009**, *11*, 4946−4948.

(20) (a) Zhao, Y.; Nakamura, R.; Kamiya, K.; Nakanishi, S.; Hashimoto, K. Nitrogen-doped carbon nanomaterials as non-metal electrocatalysts for water oxidation. *Nat. Commun.* **2013**, *4*, 2390. (b) Ding, W.; Li, L.; Xiong, K.; Wang, Y.; Li, W.; Nie, Y.; Chen, S.; Qi, X.; Wei, Z. Shape fixing via salt recrystallization: a morphology-controlled approach to convert nanostructured polymer to carbon nanomaterial as a highly active catalyst for oxygen reduction reaction. *J. Am. Chem. Soc.* **2015**, *137*, 5414−5420.

(21) Tian, G.-L.; Zhao, M.-Q.; Yu, D.; Kong, X.-Y.; Huang, J.-Q.; Zhang, Q.; Wei, F. Nitrogen-Doped Graphene/Carbon Nanotube Hybrids: In Situ Formation on Bifunctional Catalysts and Their Superior Electrocatalytic Activity for Oxygen Evolution/Reduction Reaction. *Small* **2014**, *10*, 2251−2259.

(22) Ma, T. Y.; Ran, J.; Dai, S.; Jaroniec, M.; Qiao, S. Z. Phosphorus-Doped Graphitic Carbon Nitrides Grown In Situ on Carbon-Fiber Paper: Flexible and Reversible Oxygen Electrodes. *Angew. Chem., Int. Ed.* **2015**, *54*, 4646−4650.

(23) (a) Kumar, P.; Boukherroub, R.; Shankar, K. Sunlight-driven water-splitting using two-dimensional carbon based semiconductors. *J. Mater. Chem. A* **2018**, *6*, 12876−12931. (b) Wang, Z.; Xiao, S.; Zhu, Z.; Long, X.; Zheng, X.; Lu, X.; Yang, S. Cobalt-Embedded Nitrogen Doped Carbon Nanotubes: A Bifunctional Catalyst for Oxygen Electrode Reactions in a Wide pH Range. *ACS Appl. Mater. Interfaces* **2015**, *7* (7), 4048−4055.

(24) (a) Zhang, X.; Chen, Y.; Wang, J.; Zhong, Q. Nitrogen and fluorine dual-doped carbon black as an efficient cathode catalyst for oxygen reduction reaction in neutral medium. *Chemistry Select* **2016**, *1*, 696−702. (b) Liu, L.; Zeng, G.; Chen, J.; Bi, L.; Dai, L.; Wen, Z. N-doped porous carbon nanosheets as pH-universal ORR electrocatalyst in various fuel cell devices. *Nano Energy* **2018**, *49*, 393−402.

(25) Gad, E. A. M.; Khairou, K. S. Physicochemical and Electronic Characteristics of Single Walled Carbon Nanotubes SWCNTs (Qualitative Approach). *J. Comput. Theor. Nanosci.* **2012**, *9* (5), 720−726.

(26) Liu, S.-W.; Su, W.-C.; Lee, C.-C.; Lin, C.-F.; Yeh, S.-C.; Chen, C.-T.; Lee, J.-H. Comparison of short and long wavelength absorption electron donor materials in C60-based planar heterojunction organic photovoltaics. *Org. Electron.* **2012**, *13* (10), 2118−2129.